Silicon Nanoparticle Ensembles for Lithium-Ion Batteries Elucidated by Small-Angle Neutron Scattering

Samson Y. Lai,*[†] Kenneth D. Knudsen,[†] Benjamin T. Sejersted,[§] Asbjørn Ulvestad,[‡] Jan Petter Mæhlen,[‡] and Alexey Y. Koposov*[‡]

[†]Department for Neutron Materials Characterization and [‡]Department of Battery Technology, Institute for Energy Technology (IFE), Instituttveien 18, NO-2007 Kjeller, Norway

[§]Department of Materials Science and Engineering, Norwegian University of Science and Technology (NTNU), NO-7491 Trondheim, Norway

S *Supporting Information*

ABSTRACT: Silicon in the form of nanoparticles has attracted significant interest in the field of lithium-ion batteries due to the enormous capability of lithium intake. In the present work we demonstrate the characterization of silicon nanoparticles using small-angle neutron scattering and complementary microscopy to elucidate the structure changes through the ball milling process with respect to the particle's functionality in lithium-ion batteries. Small-angle neutron scattering is a unique method for analysis of the nanoparticles as an ensemble, providing information which is often not accessible by the conventional methods for characterization of silicon nanoparticles such as microscopy. Herein we demonstrate that the analysis of neutron scattering allows to extract the specific surface area for silicon nanoparticles which was found to correlate with the first cycle Coulombic efficiency of the corresponding lithium-ion battery. In addition, using neutron scattering and electrochemical evaluation, we demonstrate that ball milling of silicon nanoparticles has different effects depending on the amorphous or crystalline nature of the material.

KEYWORDS: *lithium-ion batteries, anode, silicon nanoparticles, small-angle neutron scattering, ball milling, characterization*
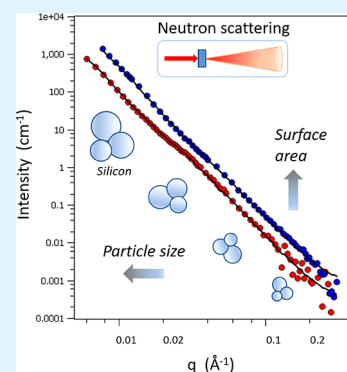
INTRODUCTION

Being one of the most abundant elements on earth, silicon possesses many valuable properties which enabled its use in various applications. Among those are solar cells as well as thin film transistors and drug delivery in medicine, to mention a few. The discovery of the potential of silicon as an anode material for Li-ion batteries (LIBs) opened a great field of research opportunities. Specifically, silicon was found to be a promising replacement of graphite—a common widely used anode material.[1] The ability to substantially increase lithium uptake of the anode originates from the formation of the silicon–lithium alloy, where one atom of silicon can accommodate on average 3.75 atoms of lithium at room temperature. That phenomenon results in a drastic improvement of the capacity with the theoretical limit of 3579 mAh/g—nearly 10 times higher than that of graphite. However, the incorporation of that many lithium atoms results in an extremely large volume change of 280%.[2] Such enormous expansion with subsequent contraction during lithiation/delithiation processes results in mechanical damage of the materials, leading to rapid degradation of electrochemical performance.[3]

The most promising pathway for mitigating the mechanical damage caused by cycling of silicon was found to be the decrease of dimensionality. The use of nanoparticles or nanowires partially dissipates the stresses associated with the expansion/contraction and therefore extends the battery lifetime.[4−7] The nanoparticles can be prepared through a variety of methods, including etching of bulk silicon,[8,9] colloidal chemistry,[10] gas chemistry,[11] or through ball milling of larger particles.[12−14] The latter, due to its low cost, availability, and high throughput yield, represents one of the most common approaches to prepare silicon at the nanoscale.[15] Early research in ball milling of crystalline Si was focused on the transition to an amorphous phase containing nanocrystallites.[13,16] Ball milling has since been utilized as a preparation step for silicon–carbon composites for lithium-ion batteries[16,17] or as a pathway for surface modification.[18] Gauthier et al. indicated that ball milling of micrometric silicon (in argon) can produce better performing silicon nanoparticles than nanosized commercial silicon.[19]

The use of various sources of silicon in combination with various treatments led to different battery performances, resulting in a large discrepancy of the results. However, despite a great variety of silicon materials available for LIBs, the set of characterization methodologies to derive structure–property correlations with respect to particle's functionality in LIBs is limited. Standard characterizations such as X-ray

diffraction (XRD) provide information about the bulk structure of the material but do not deliver necessary information about the particle size and morphology, at least not for the broad size ranges and the fractions of amorphous material encountered in Si material made for LIBs. The conventional techniques prior to (or in rare cases during) electrochemical characterization typically involve scanning electron microscopy (SEM) or transmission electron microscopy (TEM).[6,20,21] Dynamic light scattering has also been applied as a tool to gain information about the particle size and size distribution.[22] The characterization of particles inside the electrode could also be performed by FIB/SEM tomography and 3-D image analysis.[23] Small-angle neutron scattering (SANS) represents a unique technique for characterizing the ensembles of particles at nanoscale.[9] Recently, the SANS technique has been successfully utilized for characterization of battery materials *ex situ* and *in situ*.[24−27] The primary information typically extracted from such analysis is the characteristic particle size, i.e., the *z*-average particle size as weighted by volume or number depending on context, and the size distribution. Within the present work we utilize SANS for the elucidation of changes occurring to different crystalline and amorphous silicon nanoparticles through ball milling and correlate these findings with their performance in LIB anodes. We show that SANS can serve as a tool complementary to the conventional microscopy techniques (e.g., SEM) and can reveal additional structural information about the battery active material which is essential for the future optimization of silicon and other materials with relevant application in LIB anodes.

RESULTS AND DISCUSSION

To cross-correlate the particle size, source, and crystallinity with the performance as anode material, four samples of silicon particles and nanoparticles were selected for the present investigation. The sample set, as summarized in Table 1,

Table 1. Characteristics of the Different Samples Investigated

	micro-Si	*e*-Si	*nano*-Si	*a*-Si
particle size	1−5 μm	1−5 μm	<100 nm	<100 nm
state	crystalline	crystalline	crystalline	amorphous

includes the following: micrometric high purity Si, characterized by particles sizes between 1 and 5 μm (*micro*-Si); micrometric electrochemical grade Si of comparable sizes (*e*-Si); nanoscale Si, with an average particle size of or below 100 nm (*nano*-Si); and nanoscale amorphous Si (*a*-Si), which was synthesized through silane pyrolysis.[11,28−32]

All samples were ball milled in the presence of air to better replicate the conditions which could be potentially scaled up later. Silicon samples before and after ball milling were characterized by SEM as illustrated in Figure 1 with micrographs of *e*-Si as a representative sample of crystalline Si and of the amorphous *a*-Si (additional images are provided in the Supporting Information). As expected, ball milling of the crystalline samples (*micro*-Si, *nano*-Si, and *e*-Si) resulted in reduced particle sizes which is clearly visualized in SEM images. This effect was particularly pronounced for *e*-Si and *micro*-Si, where the initial particles were micrometer-sized before ball milling and nanosized after. In contrast, *a*-Si upon ball milling demonstrated partial formation of micrometer-size aggregates, while the original particles had dimensions on the

nanometer scale. However, as mentioned in the Introduction, the microscopy analysis usually does not provide the complete information about all particles present in the sample. Therefore, after preliminary microscopy evaluation the samples were analyzed using SANS.

SANS is a technique which can be utilized to investigate nanoscale structural features and to follow changes occurring in a material due to different handling and processing methods as well as resulting from changes occurring *in situ*.[33] This technique is sensitive to structural features and changes on the scale from ca. 1 to 100 nm if such produce a local variation in either the mass density or the relative composition of the material. Modifications in surface structure of particles or crystallites can also be probed via a fractal dimension parameter and/or the specific surface area. Thus, for crystalline materials the information obtained by SANS can be important for correlating modifications occurring on the atomic scales, as probed with diffraction, with structural changes on the nanoscale. For materials without a crystalline character, or with crystallites of size below 5−10 nm, the diffraction methods may not be sensitive to minor structural changes, and SANS (or SAXS, the equivalent method based on X-ray scattering) is an effective, if not the only, technique of extracting bulk information about the particle structure and features at the nanoscale.[34−36] For the samples such as *micro*-Si and *e*-Si, where the initial primary particle sizes were above the range of SANS, this technique helps to determine the sizes of the surface features typically not observable by other methods.

The SANS profiles are shown in Figure 2, which for the pristine *micro*-Si, *nano*-Si, and *e*-Si were nearly the same. While similarities were expected between *micro*-Si and *e*-Si due to their sizes being above the probing range typically accessible by SANS (from 1 to ~100 nm), the *nano*-Si profile was not expected to be featureless. However, there were no resolvable plateaus in the signal corresponding to characteristic particle sizes; instead, the linearity of the scattering curve indicated a broad distribution of particle sizes. In contrast, the sample of *a*-Si showed a noticeable deviation from linearity at $q = 0.03$ Å^{-1} (see also Figure 3 and Figure S2), demonstrating the presence of a dominant characteristic particle size of 30−40 nm (assuming spherical particles with a diameter of approximately $2\pi/q$). Despite that, the linear part of the scattering curve indicated the presence of a broad particle size distribution in the sample of *a*-Si. The details of acquisition and fitting of the SANS data are described in the Supporting Information.

As mentioned above, ball milling changes the sizes and size distribution of the particles, typically resulting in more particles at the nanoscale, which should be reflected in the SANS scattering profile. After ball milling, despite the substantial reduction in sizes as observed in SEM, the SANS of the *micro*-Si and *e*-Si samples do not show any plateau in the data (Figure 2), which would be expected if the process led to formation of a preferred particle size at the nanoscale. Instead, the signal intensity for those two samples broadly increased across the entire *q*-range (with nearly unchanged slope), indicating a greater number of small particles formed by the milling of larger particles without formation of a preferred particle size. This is equivalent to an overall increase in the specific surface area for these samples, which will be discussed later. The intensity for the *nano*-Si sample increased only in the high *q*-range, suggesting the preferential formation of smaller particles. The slight drop in intensity seen at low *q* (below ca. 0.02 Å^{-1}) after ball milling for this sample indicates a corresponding
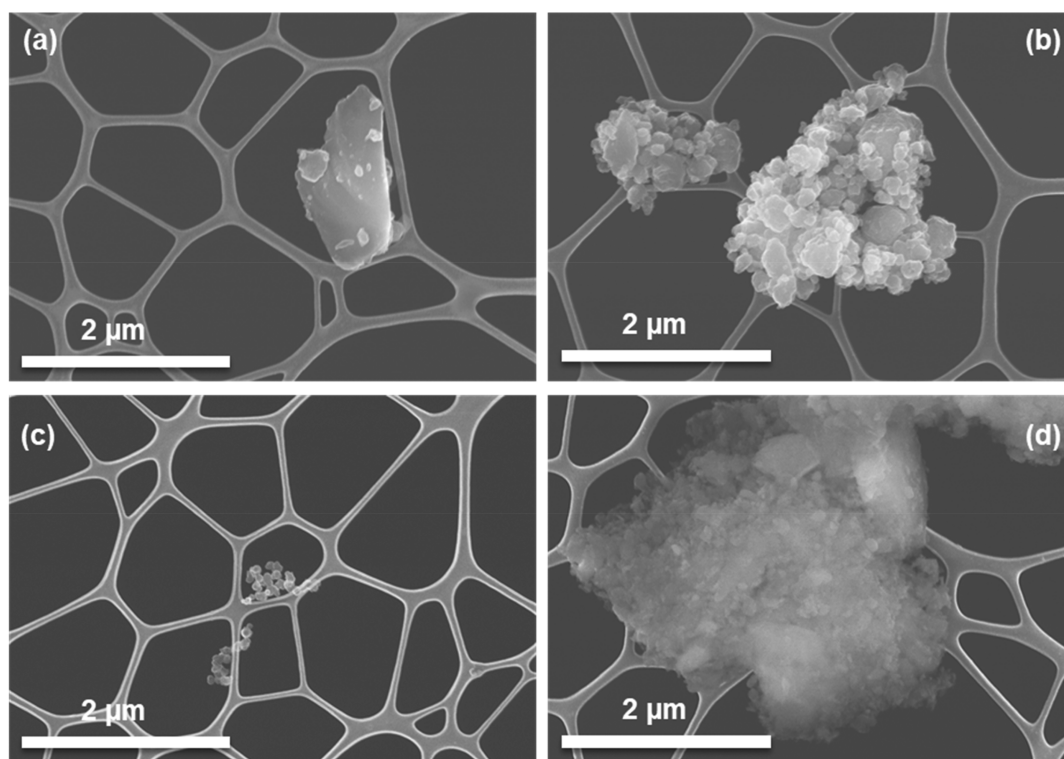
Figure 1. SEM images for (a) pristine *e*-Si, (b) *e*-Si after ball milling, (c) *a*-Si as synthesized, and (d) *a*-Si after ball milling.

reduced fraction of the larger particles. This is understandable since the average particle size (APS) of pristine *nano*-Si is 100 nm or less, and it does not contain any larger particles that could be broken down by milling and provide a SANS signal in this range. This also confirms the earlier observations of the changes in size distribution after ball milling of small particles.[19]

Interestingly, the amorphous *a*-Si undergoes more dramatic changes than the crystalline samples as reflected by its SANS profile. After ball milling the slight plateau around 0.03 Å^{-1} that existed in the pristine sample due to a characteristic particle size (cf. dashed area in Figure 2) was lost, and the signal intensity at high *q* was increased substantially more than observed for the *nano*-Si. The additional increase can be explained through the following mechanisms: upon ball milling of the amorphous silicon, the formation of the smaller particles was accompanied by formation of a highly activated surfaces, which results in greater oxidation and possible water absorption on the surface. Small particle formation and the presence of additional light elements both contribute to the increase observed in the SANS signal at high *q* for *a*-Si.

Besides general information about the particle sizes typically extracted from a SANS measurement, the specific surface area can also be estimated from the analysis of the scattering data. The specific surface area is the internal surface area (cm^2) per volume unit (cm^3) of the material, which can be translated to surface area per gram if the mass density of the material is known. This is particularly useful for nanomaterials and materials whose surface is expected to participate in chemical transformations. The specific surface area can be calculated by considering that in the high-*q* range the SANS intensity is proportional to the surface per volume unit, S_V:

$$d\Sigma/d\Omega_{q\to\infty} = (2\pi|\Delta\rho|^2 S_V)/q^4 + \text{bgd} \qquad (1)$$

where $d\Sigma/d\Omega$ is the normalized SANS intensity (in units of cm^{-1}), $\Delta\rho$ is the difference in scattering length density between the material and the surrounding matrix, and the bgd term is the incoherent background. Thus, if one plots $q^4(d\Sigma/d\Omega)$ vs q^4, S_V can be found from the intercept of the regression line with the vertical axis. Further details of the calculations and detailed results are presented in the Supporting Information. It should be noted that small-angle scattering using X-rays (SAXS) would be an alternative to SANS, but SANS has the advantage that accurate absolute normalization is straightforward (data in units of cm^2/g), allowing for a more direct calculation of the surface area. For all crystalline samples, the specific surface area increased after ball milling, while it was nearly unchanged for the amorphous sample. In addition to SANS measurements, estimation of surface area by BET was also performed and collected in Table S3. For *micro*- and *nano*-Si, the trends observed by SANS were confirmed by BET according to expectation. However, for *e*-Si and in particular *a*-Si the changes in surface area after ball milling measured by BET were quite different. We explain this by sintering of particles, formation of internal cavities (not measurable by BET), and formation of very small SiO$_2$ nanoparticles, complicating the analysis of SANS for *a*-Si after ball milling. It should also be noted that the SANS analysis is not sensitive to the presence of larger agglomerates formed during ball milling.

Further insights into the structure and morphology of the Si particles before and after ball-milling could be gained from the analysis of the particle size distribution. Knowledge of the particle size of the active material is particularly valuable, as the mechanical stability and electrochemical performance of Si-based anodes are dependent on the size of the primary particles.[37] SANS represents a method that allows one to extract the particle size distribution for the ensemble of
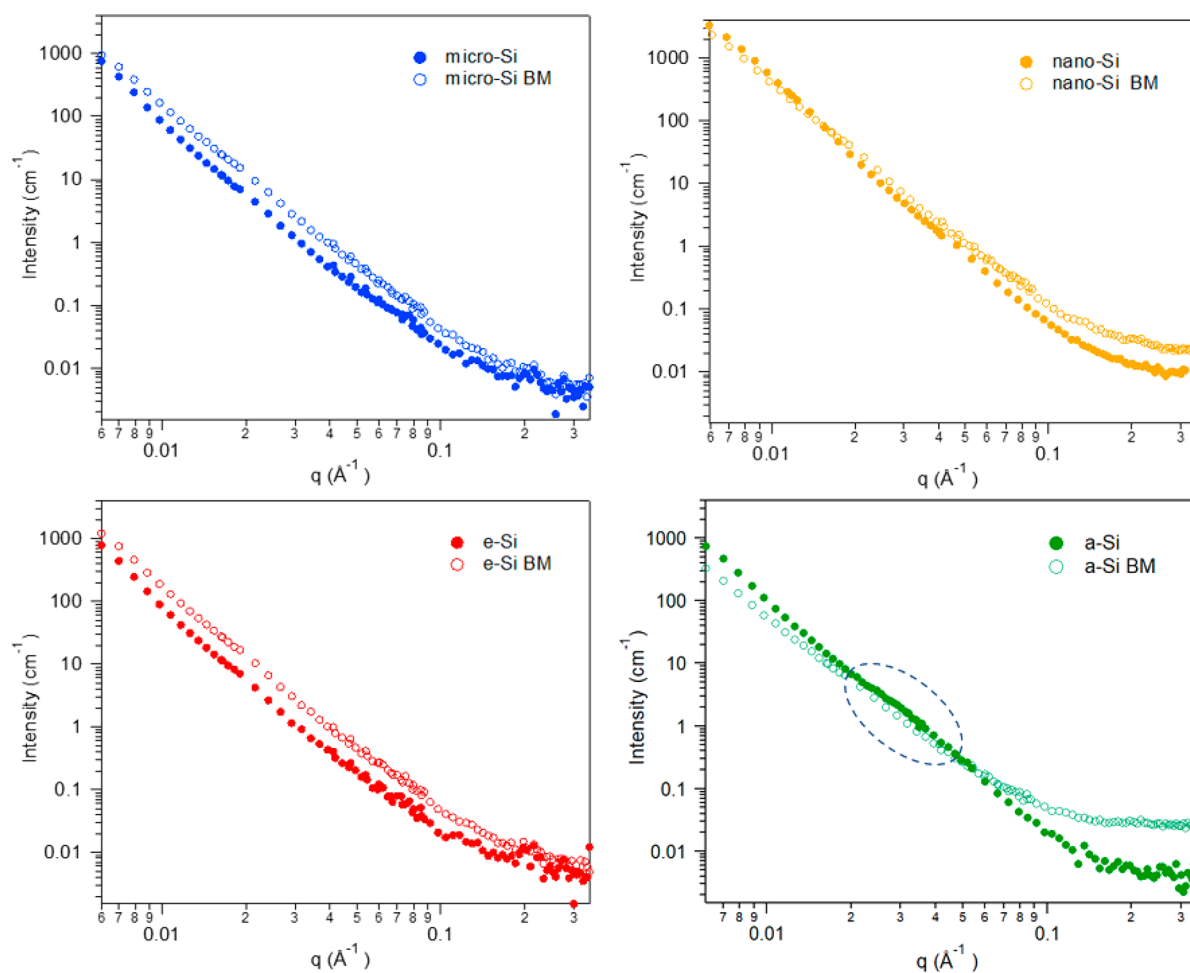
Figure 2. Small-angle neutron scattering for Si samples before and after ball milling (BM). The dashed curve in the plot for *a*-Si shows a specific contribution to the overall intensity from particles with a size centered around a diameter of 30−40 nm.
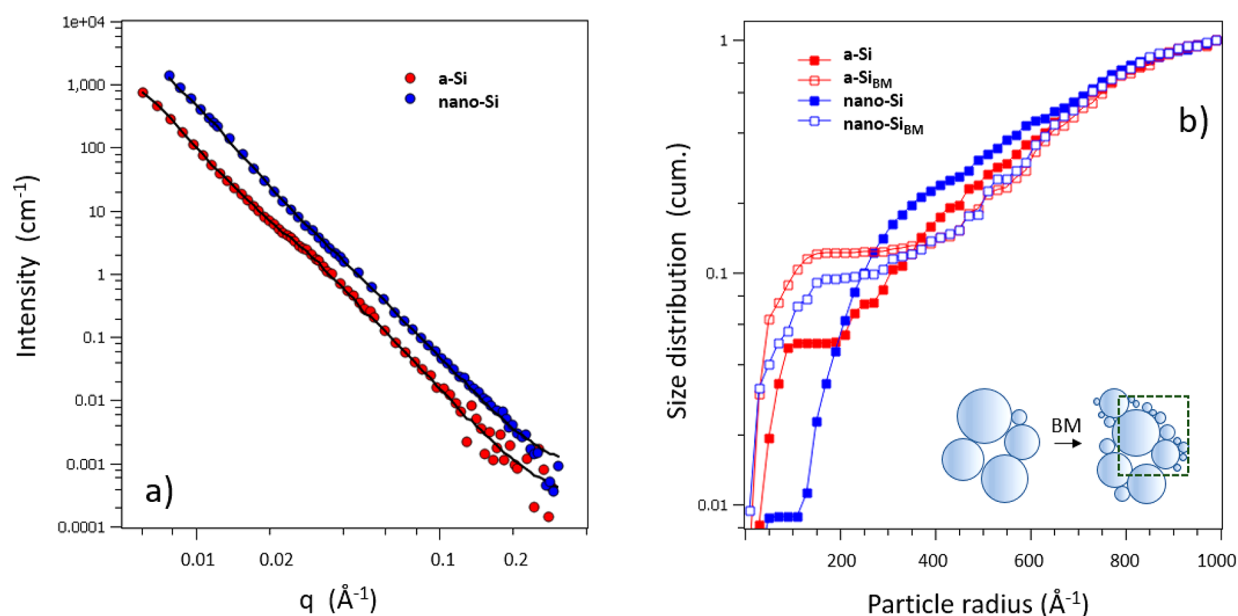
Figure 3. (a) SANS data for *a*-Si and *nano*-Si before ball milling with corresponding fits (continuous lines) based on size distributions obtained via a Monte Carlo analysis. (b) Particle sizes (particle volume) plotted as cumulative distributions. A log scale was used in these plots to better show the changes taking place in the lowest size range. Inset: illustration showing how smaller particles that are generated from ball milling will result in an increase in the effective surface area (cm^2/g) within the size range that can be probed by SANS (cf. dashed box).
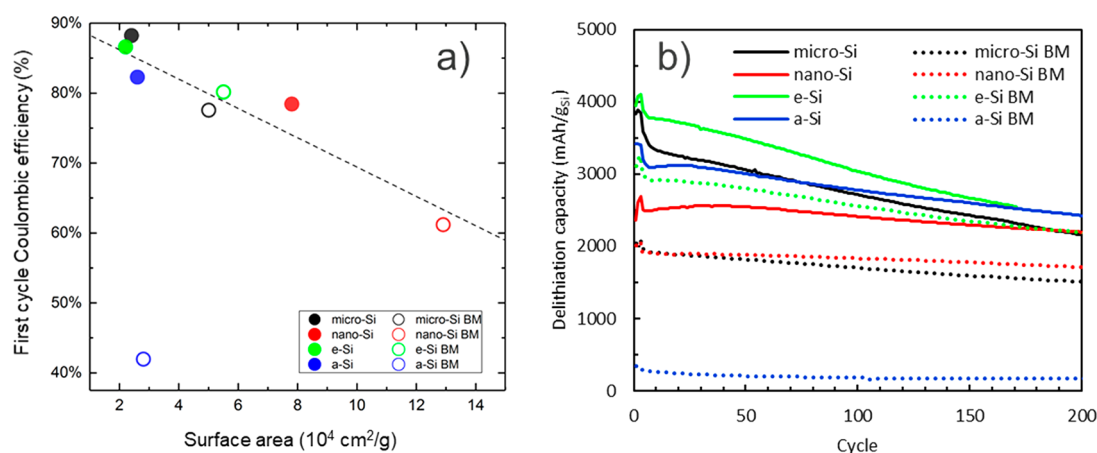
Figure 4. (a) First-cycle Coulombic efficiency as correlated to specific surface area calculated from SANS curve fitting. (b) Cycling performance for all types of Si.

particles. Specifically, the information about size distributions could be obtained from SANS via a Monte Carlo regression analysis as described by Bressler et al.[38] Figure 3a shows the SANS data for *a*-Si and *nano*-Si before ball milling with fits from which the corresponding size distributions could be extracted (Figure 3b). The analysis assumes particles with a spherical shape and a size within the range accessible by SANS, with the upper limit set to 1000 Å. The incoherent background was subtracted from the SANS data before the analysis.

Figure 3b demonstrates that pristine *a*-Si has relatively more particles with radius around 100 Å (corresponding to a diameter of 200 Å) than the pristine commercial *nano*-Si. The plot also presents the corresponding size distribution for *a*-Si$_{BM}$, showing that the number of particles in the lowest size range have increased after ball milling. The effect of ball milling on the particle size distribution was also similar for *nano*-Si$_{BM}$.

To utilize the information obtained through the combination of SANS and electron microscopy, it would be important to correlate it with the electrochemical performance of the corresponding Si-based anodes. To assess such correlation, a set of half-cells based on Si nanoparticles were fabricated and tested. This is particularly necessary to gain the understanding of which material type and postprocessing would be beneficial for Si as a material for LIB anodes.

The initial steps of lithiation/delithiation in battery anodes strongly depend on the surface of the active material participating in this electrochemical transformation. This should be reflected in the Coulombic efficiency (CE), specifically that of the first cycle, where the formation of the solid electrolyte interphase (SEI) typically takes place. The specific surface area calculated earlier from SANS was found to increase after ball milling for the whole ensemble of crystalline silicon particles due to formation of smaller particles and increased number of nanoscaled surface features. This increase is accordingly reflected in the decrease of Coulombic efficiency as visualized in Figure 4a. Therefore, for crystalline samples, the specific surface area estimations for silicon nanoparticles from SANS data represent a relevant characteristic which can be effectively utilized to predict the initial behavior of the silicon-based batteries. However, this approach will be strictly limited to a particular size range, and such an increase only reflects the changes at the nanoscale.

According to SANS data, the ball milling of *a*-Si did not change significantly the specific surface area, while noticeable changes could be observed in the microscopy studies. Clearly, the formation of small particles, in the range below 10 nm, can provide partial explanation for the changes in the SANS pattern (as can be seen in Figure 2, lower right panel). However, considering the SEM imaging results, the formation of large aggregates from smaller particles is also evident. We believe those were formed by fusing together smaller particles during the ball milling of *a*-Si. Such formation of two populations of particles through ball milling has been reported previously, however, for crystalline silicon.[19] In the case of amorphous Si, we believe that the mechanism of such change was different: The ball milling proceeds with two competing processes: formation of smaller particles, which can either oxidize or undergo the fusing process to create larger particles. The oxidized particles may not participate in the formation of the larger aggregates as was suggested recently in the literature.[39] Therefore, because of the widening of the size distribution, the average specific surface area for *a*-Si is nearly unchanged after ball milling. The formation of the small nanoparticles of *a*-Si is also accompanied by oxidation, which results in higher intensity of the SANS signal in the high-*q* limit (Figure 2) and also confirmed by the size distribution analysis (Figure 3b). In addition, the presence of highly oxidized particles will negatively affect the battery performance, which is clearly indicated by the large drop of CE after ball milling (Figure 4a).

As expected, using particles from different silicon sources as well as applying ball milling had dramatic effects on the stability of the battery anodes, as illustrated by the cycling lifetime in Figure 4b. For all crystalline samples, the ball milling negatively affected the initial anode capacity, though it simultaneously reduced the rate of the capacity degradation. Again, *a*-Si demonstrated a different behavior: after ball milling, the performance of the anodes was reduced to a level not greater than the performance of graphite. The formation of two types of particles—extremely small (most likely oxidized) and very large—was the most likely the reason for the diminished capacity and CE after ball milling of *a*-Si. The changes of the electrochemical performance upon ball milling might be attributed to the surface changes occurring during the milling process as surface chemistry dictates the binder bonding.[40] However, the analysis of the particle's surfaces confirmed the presence of oxide passivating the surface before and after ball milling (Figure S5). The TEM with elemental composition
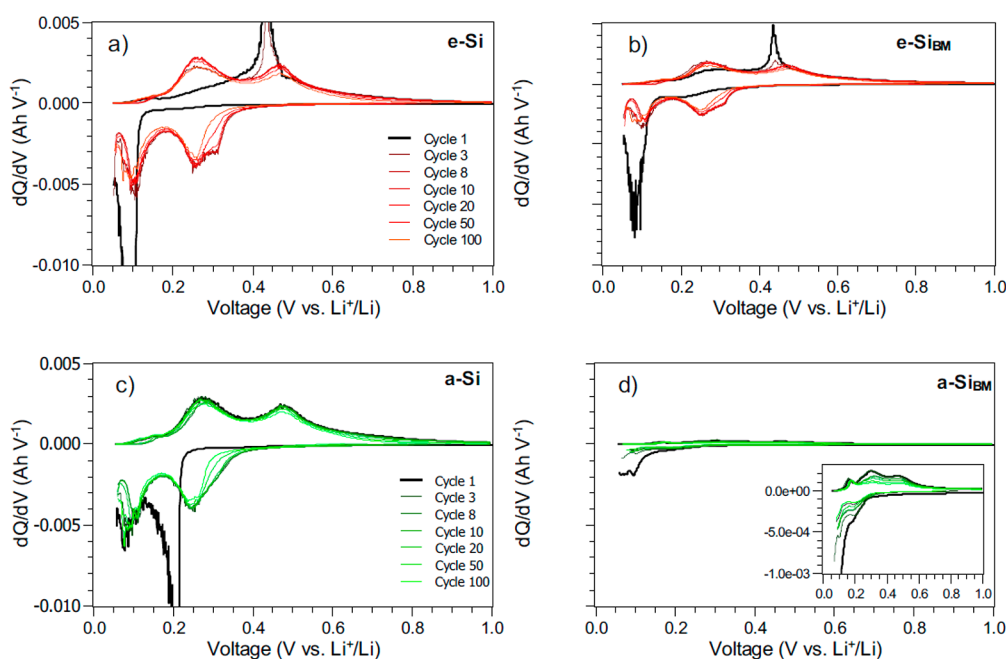
Figure 5. Differential capacity plots for (a) pristine *e*-Si (crystalline) and (b) after ball milling and (c) pristine *a*-Si (amorphous) and (d) after ball milling. For better visualization, an expanded plot for *a*-Si$_{BM}$ is included as an inset.

analysis confirmed the substantially increased amount of oxygen after ball-milling. The TEM images with elemental mapping are presented in the Supporting Information.

Additional structural information complementary to SANS and microscopy studies was extracted from the electrochemical behavior of the anode active material. For instance, the differential capacity often provides additional information about the chemical nature of the processes taking place during lithiation/delithiation. Figure 5 demonstrates examples of such measurements for the most representative samples: *e*-Si (crystalline) and *a*-Si (amorphous). Similar plots for *nano*-Si and *micro*-Si (both demonstrated behavior similar to *e*-Si) are shown in Figure S6. The main difference between the samples is in their respective first lithiation and delithiation step—that step is the most structure dependent, as further cycling of the crystalline Si leads to amorphous phase formation.[41] In particular, the initial lithiation for the crystalline Si requires more energy than for amorphous Si due to the more defective structure of the latter. The difference is reflected in the difference in lithiation voltage: 0.11 V for crystalline and 0.21 V for amorphous. Furthermore, the initial lithiation step for the crystalline material results in the formation of the crystalline phase of Li$_{15}$Si$_4$, which is reflected by the presence of the sharp peak at 0.44 V in the delithiation curve.[42] The formation of such phase was hypothesized by the presence of preordered clusters in the lithiated crystalline material which serve as nucleation sites for the Li$_{15}$Si$_4$ phase formation. As noted in earlier work, after the first formation cycles the crystalline material becomes amorphous and behaves accordingly,[19,43] which is clearly reflected by the similar profiles of differential capacity for *e*-Si and *a*-Si.[19,43]

Differential capacity also reveals the changes occurring with the materials after ball milling. For instance, the ball milling of *a*-Si, as mentioned above, led to destruction of the structure of the active anode material, which was confirmed by an extremely small lithiation capacity and almost negligible delithiation compared to the pristine material (Figure 5d).

Lithiation still occurred during the following few cycles but was barely noticeable compared to the original sample. Such large irreversibility in lithiation can suggest significant SEI formation on the surface of the remaining silicon, which ultimately leads to complete disability of the active material. On the other hand, crystalline silicon (*e*-Si) after ball milling demonstrated a stable behavior. Specifically, the lithiation and delithiation during the first cycle demonstrate a superposition of patterns characteristic for crystalline and amorphous silicon, which is reflected by the change of the lithiation profile and substantially diminished peak at 0.44 V in the delithiation curve. The position of the two peaks in the lithiation curve is quite close to the potentials of crystalline (∼0.11 V) and amorphous (∼0.25 V) lithiation peaks for the first cycle. These peaks indirectly confirm some of the observations made earlier, which suggested that ball milling of crystalline Si results in the formation of amorphous material.[12,13] Partial amorphization was also confirmed by observing significant peak broadening in X-ray diffraction (Figure S7). In addition, the lithiation profile indirectly confirms the formation of core/shell structures, with crystalline core and amorphous shell.[43] Moreover, ball milling of crystalline material performed in the presence of oxygen (air) will result in the formation of an oxide shell on the surface of the particles, which prevents further sintering and formation of larger agglomerates. However, that was not the case of amorphous Si as discussed above. We speculate that such differences are due to the different degree of breakdown during ball milling of the particles and the thickness of the oxide layer on amorphous particles. SEM also supports the formation of agglomerates, which may be easier to form due to the less dense and more defective structure of amorphous Si.

◼ CONCLUSIONS

In conclusion, herein we demonstrate the potential of SANS as a complementary characterization technique for the analysis of silicon particles as anode active materials for LIBs. SANS can serve as a parallel method to conventional electron microscopy

and X-ray diffraction revealing useful information about the ensemble of the particles and allowing to obtain the specific surface area of the material and size distribution, which can be affected by postprocessing treatments such as ball milling. The ball milling of silicon proceeds differently for amorphous and crystalline silicon: while crystalline silicon forms structures with crystalline and amorphous fractions resulting in slightly diminished anode capacity and slower degradation rates, the ball milling of amorphous silicon leads to almost complete destruction of its usability as a battery material.

■ METHODS

Silicon Nanoparticles Synthesis and Characterization. Both *micro*-Si and *nano*-Si were purchased from Alfa Aesar; *e*-Si was obtained from Elkem (Norway), and *a*-Si was prepared through silane pyrolysis as it has been described previously.[32] Silane and other gases (99.999% purity) were purchased from Praxair. *Note: special precautions should be in place while handling silane gas due to its hazardous pyrophoric behavior in air.*

All manipulations with the silicon particles were performed under ambient conditions. Ball milling was done by a planetary ball mill (Pulverisette 6, Fritsch) at 800 rpm for 20 min (loaded in air) with zirconia balls (3 mm diameter) and zirconia vial and a 25:1 ball-to-powder mass ratio. 200 mg of Si particles was used for each Si type. For SEM characterization, silicon nanoparticle samples were dispersed in ethanol solution, ultrasonicated, and pipetted onto TEM grids. SEM analysis was performed on the TEM grids using a Hitachi S-4800 instrument operating at 30 kV equipped with a retractable transmission detector (so-called low voltage STEM). X-ray diffraction (XRD) was performed with a one-dimensional LynxEye detector on a Bruker D8 Advance diffractometer (Cu $K\alpha_1, \alpha_2$ radiation). XRD samples were loaded in 0.5 mm diameter quartz glass capillaries. Transmission electron microscopy (TEM) analysis was conducted using a probe corrected instrument FEI Titan G2 60-300 equipped with a FEI SuperX energy dispersive spectrometer (EDS) and a Gatan GIF Quantum 965 electron energy loss spectrometer (EELS) and operated in scanning mode (STEM) at an acceleration voltage of 300 kV.

Battery Cell Fabrication. All the slurries for battery electrodes fabrication were prepared using the following general procedure: 15 wt % binder (sodium carboxymethyl cellulose, average $M_w \sim 90000$, Aldrich), 10 wt % graphite (TIMCAL KS6 L), 15 wt % carbon black (TIMCAL Super C65), and 60 wt % silicon (later defined as the active material) were used. The procedure was adopted from early work[44] and modified to accommodate the amounts used in the present work. Each slurry was made using ca. 150 mg of Si. The binder was dissolved in buffer solution (pH of 2.87) prepared from KOH, citric acid, and deionized water (0.7 mL) using a Thinky mixer (ARE-250CE, Thinky Co.). Then, graphite, carbon black, silicon, and an additional 0.3 mL of deionized water were added and mixed again. The slurry was then mixed using an ultrasonic mixer (Sonopuls HD2070, Bandelin Electronic) for six cycles each consisting of 2 min mixing at frequency mode 2 at 10% power.

The slurry was tape casted in repeated layers onto an 18 μm thick dendritic copper foil (SE-Cu58, Schlenk) with a blade setting of 76.2 μm (3 milli-inch) using a mini-coater (MC20, Hohsen). After casting and drying overnight, the electrodes were dried in a vacuum oven at 120 °C for 3 h before being punched into 15 mm discs and weighed. Half-cells were then made in an Ar-filled glovebox (MBraun) with <0.1 ppm of oxygen and water vapor, using Li foil as the counter electrode (99.99%, LinYi Gelon LIB Co., 15 mm in diameter and 0.250 mm thick), CR2032 stainless steel casing (Hohsen), and 18 mm disc of monolayer polypropylene (Celgard 2400, 25 μm thick) as separator.

Active material loading varied from 0.09 to 0.15 mg/cm². Four cells for a given silicon nanoparticle batch were assembled. The electrolyte (~35 μL per cell) was a custom mixture from Solvionics consisting of 1.2 M LiPF$_6$ in 3:7 ethylene carbonate:ethyl methyl carbonate (EC:EMC), respectively, with 10 wt % of fluoroethylene carbonate (FEC) and 2 wt % of vinylene carbonate (VC) as additives. The half-cells were tested using an Arbin BT-2000 cell tester between 0.05 and 1.0 V vs Li$^+$/Li with three initial formation cycles at C/20 (0.18 A/g$_{Si}$) followed by continuous cycling at C/10 (0.36 A/g$_{Si}$).

SANS Measurements. The SANS experiments were performed at the JEEP II reactor at Kjeller, Norway. The *q*-range employed in the experiments was 0.008−0.35 Å^{-1}. The samples were filled in 1 mm quartz cuvettes (Hellma Analytics), which were placed onto a copper base in the sample chamber. The space between the samples and the detector was evacuated to reduce air scattering. For all samples it was ensured that the transmission was sufficiently high (>90%) to disregard multiple scattering. Standard reductions of the scattering data, including transmission corrections, were conducted by incorporating data collected from an empty cell, a beam without cell, and blocked-beam background. The data were transformed to an absolute scale (dΣ/dΩ) by calculating the normalized scattered intensity from direct beam measurements.

■ ASSOCIATED CONTENT

Ⓢ Supporting Information

The Supporting Information is available free of charge on the ACS Publications website at DOI: 10.1021/acsaem.9b00071.

> Additional SEM figures, SANS profiles, complete pattern fits, extraction of parameters from the fits, details of the specific surface area calculations, XRD, and additional differential capacity plots (PDF)

■ AUTHOR INFORMATION

Corresponding Authors

*E-mail Alexey.Koposov@ife.no.
*E-mail Samson.Yuxiu.Lai@ife.no.

ORCID Ⓘ

Alexey Y. Koposov: 0000-0001-5898-3204

Notes

The authors declare no competing financial interest.

■ ABBREVIATIONS

LIB, lithium-ion battery; CE, Coulombic efficiency; SEI, solid electrolyte interphase; SANS, small-angle neutron scattering.

■ REFERENCES

(1) Lee, J. K.; Oh, C.; Kim, N.; Hwang, J.-Y.; Sun, Y.-K. Rational design of silicon-based composites for high-energy storage devices. *J. Mater. Chem. A* **2016**, *4* (15), 5366−5384.

(2) Obrovac, M. N.; Christensen, L. Structural Changes in Silicon Anodes during Lithium Insertion/Extraction. *Electrochem. Solid-State Lett.* **2004**, *7* (5), A93−A96.

(3) Ryu, J. H.; Kim, J. W.; Sung, Y.-E.; Oh, S. M. Failure Modes of Silicon Powder Negative Electrode in Lithium Secondary Batteries. *Electrochem. Solid-State Lett.* **2004**, *7* (10), A306−A309.

(4) Graetz, J.; Ahn, C. C.; Yazami, R.; Fultz, B. Highly Reversible Lithium Storage in Nanostructured Silicon. *Electrochem. Solid-State Lett.* **2003**, *6* (9), A194−A197.

(5) Kim, H.; Seo, M.; Park, M.-H.; Cho, J. A Critical Size of Silicon Nano-Anodes for Lithium Rechargeable Batteries. *Angew. Chem., Int. Ed.* **2010**, *49* (12), 2146−2149.

(6) Liu, X. H.; Zhong, L.; Huang, S.; Mao, S. X.; Zhu, T.; Huang, J. Y. Size-Dependent Fracture of Silicon Nanoparticles During Lithiation. *ACS Nano* **2012**, *6* (2), 1522−1531.

(7) Chakrapani, V.; Rusli, F.; Filler, M. A.; Kohl, P. A. Silicon nanowire anode: Improved battery life with capacity-limited cycling. *J. Power Sources* **2012**, *205*, 433−438.

(8) Heinrich, J. L.; Curtis, C. L.; Credo, G. M.; Sailor, M. J.; Kavanagh, K. L. Luminescent Colloidal Silicon Suspensions from Porous Silicon. *Science* **1992**, *255* (5040), 66.

(9) Choi, J.; Tung, S.-H.; Wang, N. S.; Reipa, V. Small-angle neutron scattering measurement of silicon nanoparticle size. *Nanotechnology* **2008**, *19* (8), 085715.

(10) Pell, L. E.; Schricker, A. D.; Mikulec, F. V.; Korgel, B. A. Synthesis of Amorphous Silicon Colloids by Trisilane Thermolysis in High Temperature Supercritical Solvents. *Langmuir* **2004**, *20* (16), 6546−6548.

(11) Körmer, R.; Jank, M. P. M.; Ryssel, H.; Schmid, H. J.; Peukert, W. Aerosol synthesis of silicon nanoparticles with narrow size distribution—Part 1: Experimental investigations. *J. Aerosol Sci.* **2010**, *41* (11), 998−1007.

(12) Shen, T. D.; Koch, C. C.; McCormick, T. L.; Nemanich, R. J.; Huang, J. Y.; Huang, J. G. The structure and property characteristics of amorphous/nanocrystalline silicon produced by ball milling. *J. Mater. Res.* **1995**, *10* (1), 139−148.

(13) Gaffet, E.; Harmelin, M. Crystal-amorphous phase transition induced by ball-milling in silicon. *J. Less-Common Met.* **1990**, *157* (2), 201−222.

(14) Hou, X.; Zhang, M.; Wang, J.; Hu, S.; Liu, X.; Shao, Z. High yield and low-cost ball milling synthesis of nano-flake Si@SiO$_2$ with small crystalline grains and abundant grain boundaries as a superior anode for Li-ion batteries. *J. Alloys Compd.* **2015**, *639*, 27−35.

(15) Szczech, J. R.; Jin, S. Nanostructured silicon for high capacity lithium battery anodes. *Energy Environ. Sci.* **2011**, *4* (1), 56−72.

(16) Wang, C. S.; Wu, G. T.; Zhang, X. B.; Qi, Z. F.; Li, W. Z. Lithium Insertion in Carbon-Silicon Composite Materials Produced by Mechanical Milling. *J. Electrochem. Soc.* **1998**, *145* (8), 2751−2758.

(17) Yang, J.; Winter, M.; Besenhard, J. O. Small particle size multiphase Li-alloy anodes for lithium-ionbatteries. *Solid State Ionics* **1996**, *90* (1), 281−287.

(18) Huang, S.; Cheong, L.-Z.; Wang, D.; Shen, C. Nanostructured Phosphorus Doped Silicon/Graphite Composite as Anode for High-Performance Lithium-Ion Batteries. *ACS Appl. Mater. Interfaces* **2017**, *9* (28), 23672−23678.

(19) Gauthier, M.; Mazouzi, D.; Reyter, D.; Lestriez, B.; Moreau, P.; Guyomard, D.; Roué, L. A low-cost and high performance ball-milled Si-based negative electrode for high-energy Li-ion batteries. *Energy Environ. Sci.* **2013**, *6* (7), 2145−2155.

(20) Gu, M.; Li, Y.; Li, X.; Hu, S.; Zhang, X.; Xu, W.; Thevuthasan, S.; Baer, D. R.; Zhang, J.-G.; Liu, J.; Wang, C. In Situ TEM Study of Lithiation Behavior of Silicon Nanoparticles Attached to and Embedded in a Carbon Matrix. *ACS Nano* **2012**, *6* (9), 8439−8447.

(21) McDowell, M. T.; Lee, S. W.; Harris, J. T.; Korgel, B. A.; Wang, C.; Nix, W. D.; Cui, Y. In Situ TEM of Two-Phase Lithiation of Amorphous Silicon Nanospheres. *Nano Lett.* **2013**, *13* (2), 758−764.

(22) Pecora, R. Dynamic Light Scattering Measurement of Nanometer Particles in Liquids. *J. Nanopart. Res.* **2000**, *2* (2), 123−131.

(23) Hernandez, C. R.; Etiemble, A.; Douillard, T.; Mazouzi, D.; Karkar, Z.; Maire, E.; Guyomard, D.; Lestriez, B.; Roué, L. A Facile and Very Effective Method to Enhance the Mechanical Strength and the Cyclability of Si-Based Electrodes for Li-Ion Batteries. *Adv. Energy Mater.* **2018**, *8* (6), 1701787.

(24) Möhl, G. E.; Metwalli, E.; Bouchet, R.; Phan, T. N. T.; Cubitt, R.; Müller-Buschbaum, P. In Operando Small-Angle Neutron Scattering Study of Single-Ion Copolymer Electrolyte for Li-Metal Batteries. *ACS Energy Lett.* **2018**, *3* (1), 1−6.

(25) Bridges, C. A.; Sun, X.-G.; Zhao, J.; Paranthaman, M. P.; Dai, S. In Situ Observation of Solid Electrolyte Interphase Formation in Ordered Mesoporous Hard Carbon by Small-Angle Neutron Scattering. *J. Phys. Chem. C* **2012**, *116* (14), 7701−7711.

(26) He, L.; Chathoth, S. M.; Melnichenko, Y. B.; Presser, V.; McDonough, J.; Gogotsi, Y. Small-angle neutron scattering characterization of the structure of nanoporous carbons for energy-related applications. *Microporous Mesoporous Mater.* **2012**, *149* (1), 46−54.

(27) Mamun, S. M.; Herstedt, M.; Oikawa, K.; Gustafsson, T.; Otomo, T.; Furusaka, M.; Kamiyama, T.; Sakaebe, H.; Edström, K. Neutron-scattering studies on carbon anode materials used in lithium-ion batteries. *Appl. Phys. A: Mater. Sci. Process.* **2002**, *74* (1), s1028−s1030.

(28) Wiggers, H.; Starke, R.; Roth, P. Silicon Particle Formation by Pyrolysis of Silane in a Hot Wall Gasphase Reactor. *Chem. Eng. Technol.* **2001**, *24* (3), 261−264.

(29) Onischuk, A. A.; Strunin, V. P.; Samoilova, R. I.; Nosov, A. V.; Ushakova, M. A.; Panfilov, V. N. Chemical composition and bond structure of aerosol particles of amorphous hydrogenated silicon forming from thermal decomposition of silane. *J. Aerosol Sci.* **1997**, *28* (8), 1425−1441.

(30) Slootman, F.; Parent, J.-C. Homogeneous gas-phase nucleation in silane pyrolysis. *J. Aerosol Sci.* **1994**, *25* (1), 15−21.

(31) Wu, J. J.; Flagan, R. C. Onset of runaway nucleation in aerosol reactors. *J. Appl. Phys.* **1987**, *61* (4), 1365−1371.

(32) Andersen, H. F.; Filtvedt, W.; Mæhlen, J. P.; Mongstad, T. T.; Kirkengen, M.; Holt, A. Production of Silicon Particles for High-Capacity Anode Material Yielding Outstanding Production Capacity. *ECS Trans.* **2014**, *62* (1), 97−105.

(33) Seidlmayer, S.; Hattendorff, J.; Buchberger, I.; Karge, L.; Gasteiger, H. A.; Gilles, R. In Operando Small-Angle Neutron Scattering (SANS) on Li-Ion Batteries. *J. Electrochem. Soc.* **2015**, *162* (2), A3116−A3125.

(34) Li, T.; Senesi, A. J.; Lee, B. Small Angle X-ray Scattering for Nanoparticle Research. *Chem. Rev.* **2016**, *116* (18), 11128−11180.

(35) Fratzl, P. Small-angle scattering in materials science - a short review of applications in alloys, ceramics and composite materials. *J. Appl. Crystallogr.* **2003**, *36* (3−1), 397−404.

(36) Chu, B.; Liu, T. Characterization of Nanoparticles by Scattering Techniques. *J. Nanopart. Res.* **2000**, *2* (1), 29−41.

(37) Tranchot, A.; Idrissi, H.; Thivel, P. X.; Roué, L. Influence of the Si particle size on the mechanical stability of Si-based electrodes evaluated by in-operando dilatometry and acoustic emission. *J. Power Sources* **2016**, *330*, 253−260.

(38) Bressler, I.; Pauw, B. R.; Thunemann, A. F. McSAS: software for the retrieval of model parameter distributions from scattering patterns. *J. Appl. Crystallogr.* **2015**, *48* (3), 962−969.

(39) Cao, Y.; Bennett, J. C.; Dunlap, R. A.; Obrovac, M. N. A Simple Synthesis Route for High-Capacity SiOx Anode Materials with Tunable Oxygen Content for Lithium-Ion Batteries. *Chem. Mater.* **2018**, *30* (21), 7418−7422.

(40) Delpuech, N.; Mazouzi, D.; Dupré, N.; Moreau, P.; Cerbelaud, M.; Bridel, J. S.; Badot, J. C.; De Vito, E.; Guyomard, D.; Lestriez, B.; Humbert, B. Critical Role of Silicon Nanoparticles Surface on Lithium Cell Electrochemical Performance Analyzed by FTIR, Raman, EELS, XPS, NMR, and BDS Spectroscopies. *J. Phys. Chem. C* **2014**, *118* (31), 17318−17331.

(41) Feng, K.; Li, M.; Liu, W.; Kashkooli, A. G.; Xiao, X.; Cai, M.; Chen, Z. Silicon-Based Anodes for Lithium-Ion Batteries: From Fundamentals to Practical Applications. *Small* **2018**, *14* (8), 1702737.

(42) Ogata, K.; Salager, E.; Kerr, C. J.; Fraser, A. E.; Ducati, C.; Morris, A. J.; Hofmann, S.; Grey, C. P. Revealing lithium−silicide phase transformations in nano-structured silicon-based lithium ion batteries via in situ NMR spectroscopy. *Nat. Commun.* **2014**, *5*, 3217.

(43) Obrovac, M. N.; Krause, L. J. Reversible Cycling of Crystalline Silicon Powder. *J. Electrochem. Soc.* **2007**, *154* (2), A103−A108.

(44) Mazouzi, D.; Lestriez, B.; Roué, L.; Guyomard, D. *Electrochem. Solid-State Lett.* **2009**, *12* (11), A215−A218.